TIME-OF-ARRIVAL ANALYSIS APPLIED TO THE SPATIALLY DISTRIBUTED ELF/VLF SOURCE REGION ABOVE HAARP

By

SHUJI FUJIMARU

A THESIS PRESENTED TO THE GRADUATE SCHOOL
OF THE UNIVERSITY OF FLORIDA IN PARTIAL FULFILLMENT
OF THE REQUIREMENTS FOR THE DEGREE OF
MASTER OF SCIENCE

UNIVERSITY OF FLORIDA

2011

To my parents and brother, Akio, Ikuyo and Yoshiki Fujimaru, and to my grandparents, Mitsuyoshi and Yuko Fujimaru and Shinako Hosozawa

ACKNOWLEDGMENTS

First of all, I would like to express my appreciation to my adviser, Dr. Robert Moore, for his encouragement, guidance, and help throughout my graduate studies. This thesis would not possibly have been completed in a professional manner without his patient and unselfish support. I also would like to thank Dr. Martin Uman and Dr. Jenshan Lin for serving as members of my thesis committee and for providing precise and prompt feedbacks to this thesis despite their busy schedules.

I am grateful to all my colleagues with whom I have shared a fulfilling research experience through my graduate school life. Especially, I would like to show my gratitude to Tong Wang, for providing helpful advice on signal processing problems; to Divya Agrawal, for fruitful discussions on plasma physics and electromagnetics; and to Michael Mitchel, for unfailing support of observational instruments.

Lastly, I owe my deepest gratitude to my parents and families in Japan for being my life support, with their unconditional love.

This work is supported by ONR grant #N000141010909 to the University of Florida and by BAE Systems contract #709372 to the University of Florida.

TABLE OF CONTENTS

LIST OF TABLES

LIST OF FIGURES

Abstract of Thesis Presented to the Graduate School
of the University of Florida in Partial Fulfillment of the
Requirements for the Degree of Master of Science

TIME-OF-ARRIVAL ANALYSIS APPLIED TO THE SPATIALLY DISTRIBUTED ELF/VLF SOURCE REGION ABOVE HAARP

By

Shuji Fujimaru

August 2011

Chair: Robert C. Moore
Major: Electrical and Computer Engineering

Electromagnetic waves in the Extremely Low Frequency (ELF, 3–3000 Hz) and the Very Low Frequency (VLF, 3–30 kHz) bands may be generated by modulated High Frequency (HF, 3–30 MHz) heating of the lower ionosphere in the presence of the naturally-forming auroral electrojet currents. This investigation experimentally studies high power radio wave interactions in the lower ionosphere and focuses on the dynamics of ELF/VLF wave generation, which has been utilized across a broad spectrum of applications such as submarine communications and ionospheric remote sensing.

This thesis melds Time-of-Arrival (TOA) analysis with ELF/VLF wave generation experiments in order to estimate the location of the dominant ELF/VLF source region and to distinguish between various ELF/VLF signal paths to the receiver. These accomplishments are a first step toward mapping the ELF/VLF source regions currents, which in turn may provide a means to increase ELF/VLF wave generation efficiency in the future. In this thesis, the application of linear TOA analysis to the non-linear ELF/VLF wave generation process is described in full detail. Experimental observations performed during research campaigns at the High Frequency Active Auroral Research Program (HAARP) in Gakona, Alaska, are compared with the predictions of an HF heating model to demonstrate that the TOA analysis method is a valid and useful measurement technique at ELF/VLF frequencies. Lastly, TOA analysis is applied to experimental observations to

extract geophysically meaningful information regarding the ionospheric absorption of modulated HF waves.

CHAPTER 1
INTRODUCTION

This work applies time-of-arrival (TOA) analysis to experimental observations of Extremely Low Frequency (ELF, 3–3000 Hz) and Very Low Frequency (VLF, 3–30 kHz) electromagnetic waves generated by modulated High Frequency (HF, 3-30 MHz) heating of the lower ionosphere. The experimental observations presented herein were performed near the High Frequency Active Auroral Research Program (HAARP) HF transmitter in Gakona, Alaska. The HAARP HF transmitter is presently the world's most powerful ionospheric heater, and with 3.6 MW of total transmitter power, it is capable of broadcasting signals with more than 1 GW of effective radiated power (ERP), depending on HF frequency. While a large variety of ionospheric modification experiments are regularly performed at HAARP, this thesis focuses on HAARP's ability to generate electromagnetic waves in the ELF/VLF band by modulated heating of the auroral electrojet current system, which is present in polar and sub-polar regions of the world.

Modulated heating of the lower ionosphere in the presence of naturally-forming current systems, such as the auroral electrojet, has been recognized as a means for producing ELF/VLF waves since the 1970's [e.g., *Getmantsev et al.*, 1974]. Recent technological advances have renewed efforts to increase the efficiency of ELF/VLF waves generated in this manner. One method to do so focuses on mapping the spatial distribution ELF/VLF source region currents within the lower ionosphere. In order to map the ELF/VLF source region currents, two problems must be addressed: 1) the wavelengths of the ELF/VLF frequencies used are several 10's of kilometers long, limiting the spatial resolution attainable by standard interferometric methods, and 2) experimental observations are complicated by the frequency-dependent effects of the Earth-ionosphere waveguide, which significantly affects ELF/VLF wave propagation. This thesis primarily addresses the second problem: it is demonstrated that TOA analysis may be employed to distinguish between line-of-sight ELF/VLF propagation and ionospherically-reflected ELF/VLF propagation. Separating the two types of propagation enables the experimental determination of the amplitude and phase of the received ELF/VLF signal as a function of time. This thesis leaves for future work the effort to convert TOA observations at multiple receiver sites to a spatial map of ELF/VLF source region currents.

This introductory chapter provides an overview of the ELF/VLF wave generation phenomenon and describes the observational instrumentation employed during experimental campaigns at HAARP. Chapter 2 details the TOA signal processing technique as it is applied to ELF/VLF observations. Chapters 3 and 4 demonstrate the utility of ELF/VLF TOA analysis using observations performed during several "proof-of-concept" experiments and during several more elaborate experiments. Lastly, Chapter 5 summarizes this thesis and suggests future directions for this research.

1.1 Ionosphere and Extremely Low Frequency/Very Low Frequency (ELF/VLF) Waves

The ionosphere is the portion of the Earth's upper atmosphere that is characterized by large concentrations of ions and electrons [*Budden*, 1985]. Figure 1-1, adapted from *Davies* [1990], shows the electron density distribution with altitude on a summer day at mid-latitudes. The ionosphere extends from about 60 km to 1000 km altitude and is divided into three general regions: the *D*-region, ranging from ~60 km to 100 km, the *E*-region, ranging from ~100 km to 140 km, and the *F*-region, ranging above ~140 km.

The charged particles within the ionosphere affect the propagation of radio waves as a function of the wave frequency. An abbreviated summary of propagation features for different frequency bands is provided by Table 1-1. As can be seen from Table 1-1, adapted from [*Davies*, 1990], lower frequency waves may propagate large distances within the Earth-ionosphere waveguide with relatively low attenuation. As a result, ELF and VLF waves have been used for such purposes as submarine communications [e.g., *Wait*, 1972] and ionospheric remote sensing [e.g., *Cummer et al.*, 1998].

The interaction between electromagnetic waves and the *D*-region ionosphere is scientifically interesting. The Earth-ionosphere waveguide is formed by the ground on one side and *D*-region ionosphere on the other. In addition, as is shown in Figure 1-2, the *D*-region has high electron-neutral collision frequencies that result in the absorption of electromagnetic waves by the ionosphere. We will explore these ionospheric plasma and wave propagation characteristics using ELF/VLF wave generation experiments at HAARP.

1.2 ELF/VLF Wave Generation and Propagation

The cartoon diagram shown in Figure 1-3 depicts the process of ELF/VLF wave generation by modulated HF heating of the lower ionosphere. The modulated HF signal broadcast upward by the HAARP HF transmitter is absorbed by the collisional D-region ionosphere at $\sim$60–100 km altitude. The wave energy absorbed by the ionosphere modifies the temperature of the constituent electrons of the ionosphere. Because the wave energy is modulated, the electron temperature is also modulated. The conductivity of the lower ionosphere strongly depends on the electron temperature. As a result, the conductivity of the lower ionosphere is modulated with the same fundamental periodicity of the HF signal modulation. This property has two significant effects: 1) the time-varying conductivity leads to a time-varying rate of absorption of the HF wave (i.e., the absorption of the HF wave modifies the rate of absorption of the HF wave – a nonlinear process known as self-absorption), and 2) the time-varying conductivity together with the background electrojet electric field yields an ELF/VLF source current density $\vec{J} = \sigma\vec{E}$. The spatially distributed ELF/VLF source currents excite the Earth-ionosphere waveguide and produce waves that may propagate to large distances around the globe. For long-distance propagation, it is typical to model Earth-ionosphere waveguide propagation using modal signal analysis, in which a discrete number of waveguide modes propagate with varying group velocities, phase velocities, and attenuation rates. For short-distance propagation, as is the case for the location of the receivers used in this work, a ray-based analysis method is employed. The two methods are mathematically equivalent. At large distances, fewer waveguide modes are necessary to calculate the received signal, whereas at short distances, fewer ray paths are required to calculate the received signal.

The following subsections provide brief descriptions of the HF propagation and absorption processes and the resulting generation and propagation of ELF/VLF waves.

1.2.1 High Frequency (HF) Propagation and Absorption

The HF wave broadcast by HAARP propagates to the lower ionosphere, in which it is refracted and partially reflected. The amount of refraction and the percentage of reflection are determined by the variation in the ionospheric refractive index along the propagation path. The refractive index of the ionospheric plasma depends on the local electron density, electron temperature, and the direction and magnitude of the Earth's magnetic field at that location. A detailed description of HF propagation through the lower ionosphere is provided by *Moore* [2007]. For the purposes of this work, it suffices to state that the ray path and group velocity of the HF wave may be determined accurately using ambient ionospheric parameters (i.e., the effects of HF heating on these properties may be neglected), while the amplitude and phase of the HF wave depend sensitively on the modulated electron temperature via conductivity.

The modulation of ionospheric electron temperature may be described by the localized energy balance equation (adapted from *Moore and Agrawal* [2011]):

$$\frac{3}{2}N_e\kappa_B\frac{dT_e}{dt} = 2k\chi(T_e)S - L(T_e, T_0) \tag{1–1}$$

The left hand side of the equation, $\frac{3}{2}N_e\kappa_B\frac{dT_e}{dt}$, represents the change in thermal ionospheric energy as a function of time for a given electron density, N_e, and electron temperature, T_e. κ_B is the Boltzmann constant. The first term of the right hand side, $2k\chi(T_e)S$ represents the power of the HF wave that is absorbed by the ionosphere, with an absorption rate $\chi(T_e)$ and HF Poynting flux S. The second term of the right hand side, $L(T_e, T_0)$ is the electron energy loss rate as a function of T_e and the ambient electron temperature T_0. For the modeling results used in this work, the equations describing $\chi(T_e)$ and $L(T_e, T_0)$ are presented by *Moore* [2007].

The modulated electron temperature results in a modulated ionospheric conductivity. In the lower ionosphere, conductivity is represented as a tensor because the relationship between $\vec{J}$ and $\vec{E}$ depends on the direction of the electric field with respect to the Earth's magnetic field. The conductivity tensor is typically expressed:

$$\bar{\bar{\sigma}} = \begin{bmatrix} \sigma_P & -\sigma_H & 0 \\ \sigma_H & \sigma_P & 0 \\ 0 & 0 & \sigma_{||} \end{bmatrix} \tag{1–2}$$

where σ_P, σ_H, and $\sigma_{||}$ denote the Pedersen, Hall, and parallel conductivities, respectively. Using a kinetic formulation, the conductivity components can be described [*Tomko*, 1981]:

$$\sigma_P = \frac{4\pi}{3} j \frac{q_e^2}{m_e \omega} \int_0^\infty \frac{U}{U^2 - Y^2} v_e^3 \frac{\partial f_{e,0}}{\partial v_e} dv_e \tag{1–3}$$

$$\sigma_H = \frac{-4\pi}{3} j \frac{q_e^2}{m_e \omega} \int_0^\infty \frac{U}{U^2 - Y^2} v_e^3 \frac{\partial f_{e,0}}{\partial v_e} dv_e \tag{1–4}$$

$$\sigma_{||} = \frac{4\pi}{3} j \frac{q_e^2}{m_e \omega} \int_0^\infty \frac{1}{U} v_e^3 \frac{\partial f_{e,0}}{\partial v_e} dv_e \tag{1–5}$$

where q_e is the electron charge, m_e is the electron mass, and ω is the angular frequency. U and Y are given:

$U = 1 - j\frac{v_{eff}}{\omega} \quad Y = \frac{\omega_{ce}}{\omega}$

v_{eff} is the effective electron-neutral collision frequency and ω_{ce} is the cyclotron frequency. $f_{e,0}$ is the Maxwellian electron velocity distribution function:

$$f_{e,0} = N_e \left(\frac{m_e}{2\pi\kappa_B T_e}\right)^{3/2} \exp\left(\frac{-m_e v_e^2}{2\kappa_B T_e}\right) \tag{1–6}$$

Hence together with auroral electrojet electric field, $\vec{E}$, the modulated conductivities become current sources (i.e., $\vec{J} = \bar{\bar{\sigma}}\vec{E}$), and constitute a source for electromagetic radiation at ELF/VLF frequencies, as described in the next subsection.

1.2.2 ELF/VLF Signal Propagation

The radiation of electromagnetic waves from a spatially distributed current source in free-space can be expressed as [*Balanis*, 1986]:

$$B_{\text{fs}}(x, y, z) = -\frac{\mu}{4\pi} \int\int\int_V (\hat{R} \times J) \frac{1 + j\beta R}{R^3} \exp^{-j\beta R} dx'dy'dz' \tag{1–7}$$

where x, y, and z represent the location of the receiver, x', y', and z' represent the location of the source, R is the distance between the receiver and source, μ is the permeability of free-space, and β is the wave propagation constant.

In order to account for Earth-ionosphere waveguide effects, however, boundary conditions must be included. A reasonable first approximation of the Earth-ionosphere waveguide is a parallel-plate waveguide with perfectly conducting walls and a plate separation, h, representing the reflection height. In such a waveguide, the received signal may be modeled using image theory. Although this representation does not account for frequency-dependent reflection heights or reflection coefficients, it will serve the purposes of the work presented herein. Using this parallel-plate representation of the Earth-ionosphere waveguide, the line-of-sight propagation path, which arrives at the receiver earliest, is equivalent to a distributed current source above a ground plane. In fact, all subsequent reflections may be represented similarly, although sourced at different altitudes. The **B**-field detected on the ground resulting from a spatially distributed current source over a ground plane may be expressed:

$$B_x = 2B_{\text{fsx}} \tag{1–8}$$

$$B_y = 2B_{\text{fsy}} \tag{1–9}$$

$$B_z = 0 \tag{1–10}$$

1.3 ELF/VLF Wave Current Sources

The spatial distribution of ELF/VLF source currents is of prime interest to the work presented in this thesis. Here we provide a background relating previous research efforts to experimentally detect ELF/VLF source current distributions.

Rietveld et al. [1984] analyzed the spatial distribution of the auroral electrojet electric field by sweeping the direction of the HF beam and comparing ELF/VLF wave observations with the direction of the electric field measured by the STARE radar. This experiment recognizes that the detected ELF/VLF waves can possibly be used to estimate the spatial distribution of the auroral electrojet electric field. Using far field measurements, *Barr et al.* [1998] and *Cohen et al.* [2008] show that aiming HF beam toward the receiver increases the ELF/VLF wave amplitude detected at the receiver. While this result is expected (since the source is closer to the receiver), the amount of amplitude increase was unexpectedly high, indicating a more efficient excitation of the Earth-ionosphere waveguide using oblique HF heating of the ionosphere, rather than a simple source-to-receiver distance reduction. On the other hand, *Barr et al.* [1998] explains that reductions of amplitudes with the HF beam aimed away from the receiver may be caused by phase spreading due to the increasing difference of propagation distance in different paths.

A number of theoretical and experimental efforts have been performed to determine the ELF/VLF wave current source location. For example, *James* [1985] theoretically computes the modulated ionospheric properties as a function of altitude with given appropriate ionospheric parameters and determines the dominant altitude of the ELF/VLF wave source. On the other hand, *Rietveld et al.* [1986] experimentally estimates the source height using pulsed ionospheric heating. *Rietveld et al.* [1989] and *Riddolls* [2003] use a method similar to time-of-arrival analysis to determine the ELF/VLF source heights (the difference from our TOA analysis is discussed in Section 2.4.3). These analyses were conducted assuming the dominant ELF/VLF source region was located directly above the HF transmitter and did not attempt to separate ionospherically-reflected signals from the line-of-sight signals. Most recently, *Payne et al.* [2007] attempted to map the ELF/VLF source current structure using an ELF/VLF interferometer chain. Tonal ELF/VLF transmissions were employed, however, and he demonstrated that in this case the problem is ill-conditioned (i.e., not solvable).

Ionospherically-reflected signals have been directly observed in ELF/VLF recordings [e.g., *Papadopoulos et al.*, 2003; *Rietveld et al.*, 1986]). It is thus possible that the experimental observations listed above may be contaminated by ionospherically-reflected signals, affecting the analysis. The TOA method presented in this work is capable of separating the line-of-sight and the ionospherically-reflected components of the observed ELF/VLF wave, and these experiments have provided the motivation to experimentally separate line-of-sight propagation from ionospheric-reflection propagation.

1.4 Observational Instrumentation

1.4.1 High Frequency Active Auroral Research Program (HAARP)

The High Frequency Active Auroral Research Program (HAARP) is a jointly-funded Air Force/Navy research facility located at Gakona, Alaska (62.39°N, 145.15°W) with the purpose to study upper atmosphere. The primary research instrument at HAARP is the HF phased array transmitter, consisting of 180 crossed dipole antennas aligned in a 12x15 grid. The total transmitter power is 3.6 MW, and the array is capable of broadcasting ERPs $>$1 GW. The available HF frequency range is 2.8 to 10 MHz. HAARP accommodates a number of modern observational instruments, such as radars, magnetometers, and optical detectors.

The HAARP HF transmitter is capable of broadcasting HF waves with various wave polarizations (e.g., circular, linear, elliptical) and using various modulation formats (e.g., AM, FM, PM). A number of modulation waveforms are available, such as square-wave, sinusoidal, triangular, saw-tooth, and pulse modulation. The main lobe of the transmission may be directed up to 30° off zenith at any azimuthal angle, and the direction of the beam may be changed anywhere within 15° of a given center point in 5-μsec intervals. It is also possible to divide the HF array into two sub-arrays that may be used to independently broadcast at different frequencies simultaneously.

For the experiments presented in this work, HAARP broadcast a 3.2 MHz (X-mode polarized) signal that was amplitude modulated using a square-wave modulation waveform.

1.4.2 ELF/VLF Receivers

During experimental research campaigns at HAARP, ELF/VLF wave observations are performed at ground-based receivers located at Sinona Creek in Chistochina, Alaska ($\sim$33 km from HAARP) and at Milepost 71 of the Tok Cutoff ($\sim$96 km from HAARP) as shown in Figure 1-5. After the recent campaign in July 2010, receivers are located at Sinona Creek and at Sportsman Paradise Lodge (a.k.a., Paradise, $\sim$100 km from HAARP).

Each receiver system records signals from two orthogonal, triangular loop antennas oriented in North-South (NS) and East-West (EW) directions to detect the horizontal magnetic field at ground level as is shown in Figure 1-6. The antenna outputs are connected to a weather-proofed preamplifier box. Using a 200–1000-ft cable, the detected signals are fed to a line receiver and digitized and stored on a computer at 100 kHz sampling frequency with 16 bit resolution. The frequency sensitivity of the system is between 500 and 49 kHz.

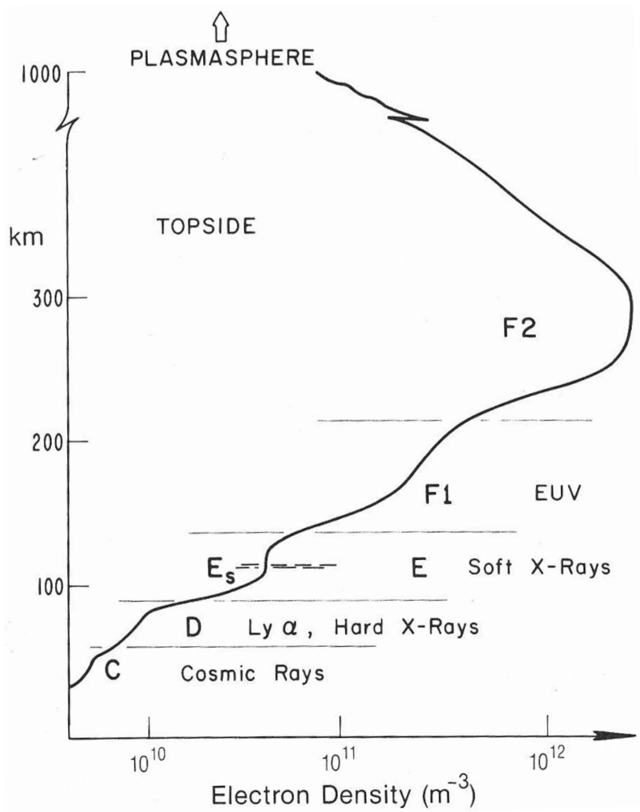

Figure 1-1. Example electron density profile as a function of altitude. Adapted from Davies, K. 1990. Ionospheric Radio, Peter Peregrinus Ltd., London, UK.

Table 1-1. Radio spectrum (adapted from Davies, K. 1990. Ionospheric Radio, Peter Peregrinus Ltd., London, UK.) Note: the frequency ranges specified below vary slightly the literature.

Name	Frequency Range	Primary Propagation Modes
Extremely Low Frequency (ELF)	<3 kHz	Earth-ionosphere waveguide, Penetrates sea water
Very Low Frequency (VLF)	3 – 30 kHz	Earth-ionosphere waveguide, Ground wave
Low Frequency (LF)	30 – 300 kHz	Waveguide, Ground wave
Medium Frequency (MF)	300 – 3000 kHz	E-region reflection (night), Ground wave
High Frequency (HF)	3 – 30 MHz	Reflection from E and F regions
Very High Frequency (VHF)	30 – 300 MHz	Line of sight, Scatter from ionosphere
Ultra High Frequency (UHF)	300 – 3000 MHz	Line of sight (affected by ionospheric irregularities)
Super High Frequency (SHF)	3 – 30 GHz	Line of sight (tropospheric, affected by ionospheric irregularities)

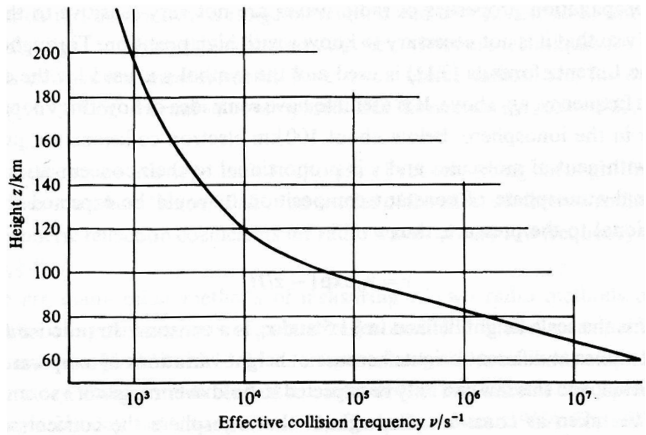

Figure 1-2. Electron collision frequency as a function of altitude adapted from Budden, K.G. 1985 The propagation of radio waves (Page 12, Figure 1-2), Cambridge University Press, Cambridge, UK.

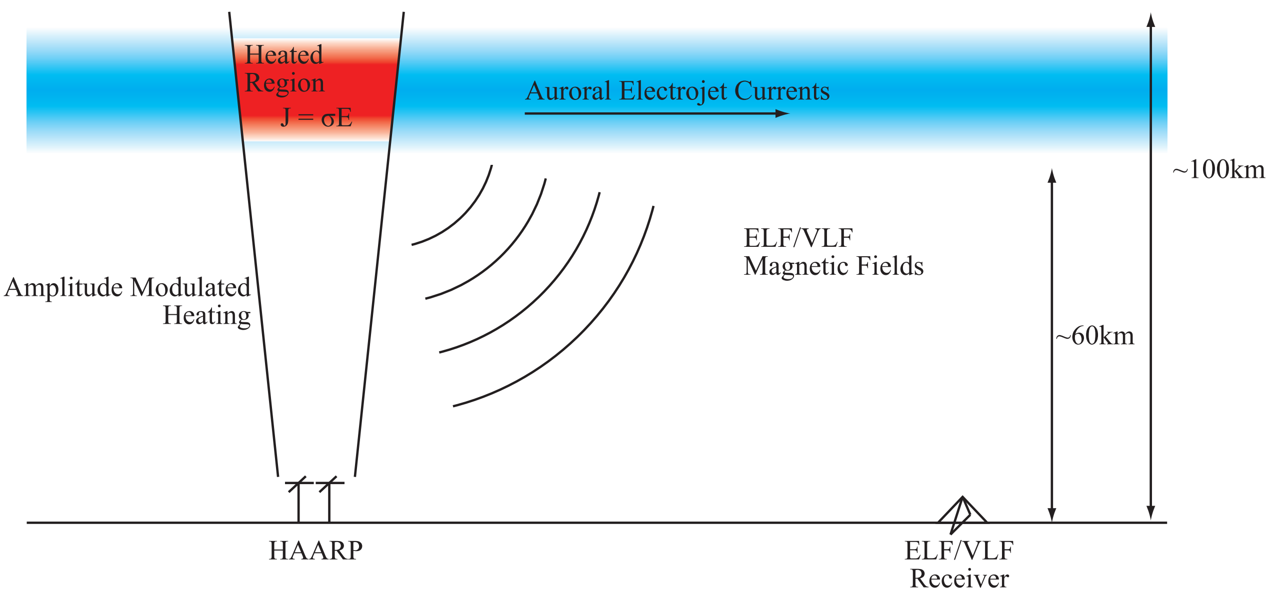

Figure 1-3. A cartoon diagram of ELF/VLF wave generation at HAARP.

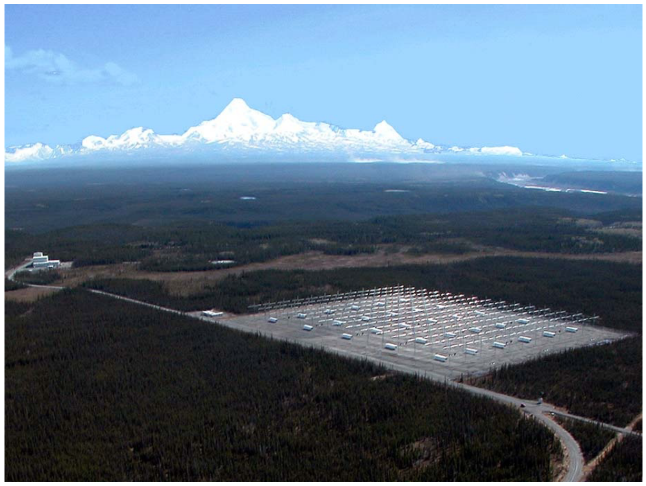

Figure 1-4. Picture of the HAARP antenna array located in Gakona, Alaska (Source:http://www.haarp.alaska.edu/haarp/images/ovhead.jpg)

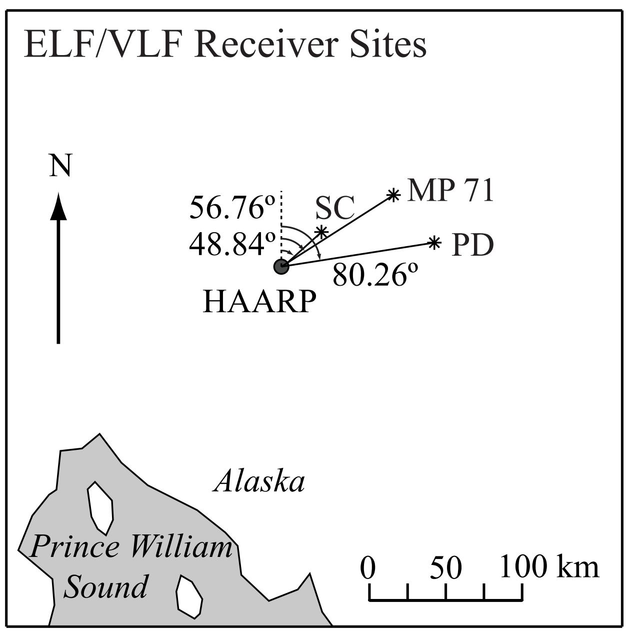

Figure 1-5. Geographic map showing the location of the ELF/VLF receiver sites used in this work in relation to the HAARP facility. SC refers to Sinona Creek; MP71 refers to Milepost 71; and PD refers to Paradise.

Figure 1-6. Picture of the ELF/VLF antenna deployed at Sportsman Paradise Lodge, Alaska(a.k.a., Paradise). A 1000-ft cable, connecting the pre-amplifier and line receiver, which is located next to the data acquisition system in a nearby cabin.

CHAPTER 2
EXPERIMENTAL METHOD: TIME-OF ARRIVAL (TOA) TECHNIQUE

This chapter describes the HF transmission schemes used for TOA analysis, together with mathematical derivations of the TOA technique. Furthermore, the TOA's timing accuracy and resolution are discussed together with it's physical and mathematical limitations.

2.1 TOA Transmission Description

The HAARP HF transmitter is used to modulate the auroral electrojet currents using square-wave amplitude modulation with linear modulation frequency ramps. For the typical experiment, the HF (carrier) frequency is 3.2 MHz (with X-mode polarization), while the modulation frequency ranges linearly from 1 kHz to 5 kHz over 4 seconds. The HF beam is oriented vertically. Over the course of several experiments, however, these parameters were modified in different combinations to investigate their effect on the TOA results. The primary transmission parameter relevant to TOA analysis is the frequency-time characteristic of the imposed modulation waveform.

2.2 Time-of-Arrival Method

The goal of the TOA method is to estimate the amplitude and phase of ELF/VLF waves arriving at the receiver as a function of time in such a way as to reveal characteristics of the ELF/VLF wave source region. As *Payne et al.* [2007] demonstrated, this is not possible using a single-tone modulation frequency. Instead, we utilize a frequency-time ramp modulation format as is described in the previous section. This type of signal is broadly known as Frequency Modulated Continuous Wave (FMCW) in radar applications [e.g., *Barrick*, 1973; *Schuster et al.*, 2006] and is commonly referred to as "chirp" modulation.

The time-dependence of the modulation frequency provides a means to differentiate between signals arriving at different times: the impulse response of the system may be directly calculated from the observations, providing a time-domain estimate of the multi-path propagation delays and other signal properties. It should be noted at this point that the ELF/VLF wave generation process is inherently nonlinear, whereas the TOA analysis method presented is linear. For instance, ELF/VLF harmonics at modulation frequencies that are not transmitted are regularly observed in ELF/VLF recordings. The implementation of the TOA analysis first separates the received ELF/VLF harmonics and considers them individually. Additionally, because ELF/VLF wave generation is nonlinear with HF power and significantly varies with HF frequency and polarization, it is expected that the calculated impulse response applies only for a given HF power, frequency, and polarization. Lastly, because different modulation waveforms produce different harmonic content when driving the ionospheric conductivity modulation, we do not expect the calculated impulse to apply to all modulation waveforms. Instead, the intent is to interpret a given TOA impulse response to yield information about the ELF/VLF source region for a given set of transmission parameters.

We begin by expressing the time-averaged HF Poynting flux of the transmission, which has a square-wave envelope, as the sum of harmonic components:

$$\langle P(t)\rangle = \sum_n \langle P_n(t)\rangle = \sum_n A_n \cos\left(2\pi n\left(f_0 t + \frac{\Delta f}{2}t^2 + \phi_{0n}\right)\right) \tag{2–1}$$

where $\langle P_n(t)\rangle$ represents the time-averaged Poynting flux of the n^{th} harmonic, f_0 is the initial frequency of the ramp, and Δf is the slope of the frequency-time ramp. A_n and ϕ_{0n} are the amplitude and phase of the n^{th} harmonic, both of which are assumed to be constant with frequency in this work.

For a given harmonic, the received signal may be expressed:

$$r_n(t) = \langle P_n(t)\rangle * g_n(t) * p(t) = \langle P_n(t)\rangle * h_n(t) \tag{2–2}$$

where $g_n(t)$ is the effective impulse response converting HF power to ionospheric current modulation for the n^{th} harmonic, $p(t)$ is the impulse response characterizing

ELF/VLF wave propagation to the receiver, and $*$ denotes convolution. TOA analysis finds $h_n(t)$, the effective impulse response combining the effects of current generation and wave propagation for a given harmonic.

The total received ELF/VLF signal, $R(t)$, may thus be expressed:

$$R(t) = \sum_n \left\{ A_n \cos\left(2\pi n \left(f_0 t + \frac{\Delta f}{2} t^2\right) + \phi_{0n}\right) * h_n(t) \right\} \sqcap (t/T - 1/2) \text{Ш}(F_s t) \tag{2–3}$$

where T is the duration of the frequency-time ramp, F_s is the sample frequency of the data acquisition system, and $\sqcap$ and Ш are defined:

$$\sqcap(t) = \begin{cases} 1 & |t| < \frac{1}{2} \\ 0 & |t| > \frac{1}{2} \end{cases} \tag{2–4}$$

$$\text{Ш}(t) = \sum_{n=-\infty}^{\infty} \delta(t - n) \tag{2–5}$$

The processing of the n^{th} harmonic begins by mixing-down and filtering the received signal. The mixing kernel for the n^{th} harmonic may be expressed:

$$m_n(t) = e^{-j2\pi n\left(f_0 t + \frac{\Delta f}{2} t^2\right)} \sqcap (t/T - 1/2) \tag{2–6}$$

The 100-Hz bandwidth low-pass filter, $b(t)$, is implemented using a 2000-tap, 8^{th}-order Kaiser window. After applying the low pass filter, the base-band signal is mixed-up to its original frequency range using the complex conjugate of $m_n(t)$, and the real component of the resulting complex-valued signal represents the isolated n^{th} harmonic.

The isolated n^{th} harmonic of the frequency-time ramp, $y_n(t)$, may then be described:

$$y_n(t) = \Re\left\{\left[(R(t) m_n(t)) * b(t)\right] m_n^*(t)\right\} \tag{2–7}$$

The impulse response, $h_n(t)$, is calculated by Fourier analysis, using $y_n(t)$ as the output signal and $x_n(t)$ as the input signal:

$$x_n(t) = \cos\left(2\pi n\left(f_0 t + \frac{\Delta f}{2}t^2\right)\right)\sqcap(t/T - 1/2)\text{Ш}(F_s t) \tag{2–8}$$

$$h_n(t) = \mathcal{F}^{-1}\left[\frac{\mathcal{F}(y_n(t))}{\mathcal{F}(x_n(t))}\sqcap\left(\frac{f - nf_0}{nT\Delta f} - \frac{1}{2}\right)\right] \tag{2–9}$$

where $\mathcal{F}$ denotes the Fourier transform and $\mathcal{F}^{-1}$ denotes the inverse Fourier transform. Note that ΔfT represents the full bandwidth traversed by the frequency-time ramps. Then, $h_n(t)$ reduces to:

$$h_n(t) = A_n(t)e^{j\phi_n(t)} * \left\{e^{j2\pi f_c t}\text{sinc}(nT\Delta ft)nT\Delta f\right\} \tag{2–10}$$

where $A_n(t)$ and $\phi_n(t)$ represent the bandwidth-averaged amplitude and phase of the received signal as a function of time, and f_c is the center frequency of the frequency-time ramp. Here, $h_n(t)$ is complex-valued in order to directly assess the phase $\phi_n(t)$. This result is achieved by eliminating the negative frequency components in Equation 2–9 [*Gabor*, 1946].

An example $h_n(t)$ is shown in Figure 2-1. As seen in Equation 2–10, the TOA result consists of the complex-weighted sum of sinc functions. Each signal arriving at the receiver at different times is convolved with a sinc function and forms the TOA result. Figure 2-1 also compares TOA results for calculations performed using only positive frequency components and those performed using both positive and negative frequency components. While the combined frequency form produces a narrower main lobe, it does not directly provide phasing information (it is entirely real-valued). Additionally, the positive-frequency (complex-valued) $h_n(t)$ represents the same information as the combined-frequency (real-valued) $h_n(t)$, due to conjugate (Hermitian) symmetry [*Boashash*, 2003]. The complex-valued form of $h_n(t)$ is used throughout this work.

As can be seen in the Equation 2–9, we apply a rectangular window in the frequency domain and transform it to the sinc function in the time domain. In the future, this window may be replaced by a different window such as a Hamming or Kaiser window, whose side lobes are suppressed to a greater extent than those of the rectangular window. In this thesis, the rectangular window is used as a matter of simplicity. The width of the sinc function is determined by the bandwidth of the frequency ramps, $\Delta f T$, and it dictates the TOA properties such as the timing accuracy and resolution.

2.3 Alternative Time-of-Arrival Derivation

The frequency-time ramp employed by our TOA method produces interesting and complicated integrals in the Fourier domain. Thus far, we have omitted providing the actual Fourier Transforms of our transmission, as these transforms may easily be calculated numerically. For completeness, we provide the following derivation in the continuous rather than the discrete time domain and show that the result is equivalent to Equation 2–10.

Let us start with Equation 2–7 and assume $h_n(t)$ has some time delay, τ, and an amplitude and phase, $A_n(\tau)e^{j\phi_n(\tau)}$.

$$y_n(t,\tau) = A_n(\tau)\cos\left(2\pi n\left(f_0(t-\tau)+\frac{\Delta f}{2}(t-\tau)^2\right)+\phi_n(\tau)\right)\sqcap\left(\frac{t-\tau}{T}-\frac{1}{2}\right) \quad (2\text{–}11)$$

Now we take a Fourier transform with respect to time, t:

$$\begin{aligned} Y_n(f,\tau) &= \mathcal{F}[y_n(t)] && (2\text{–}12)\\ &= \int_{\tau}^{\tau+T} y_n(t)e^{-j2\pi ft}\,dt && (2\text{–}13)\end{aligned}$$

Using Euler's formula,

$$
\begin{aligned}
&Y_n(f,\tau) = \\
&\quad \frac{A_n(\tau)}{2}\int_{\tau}^{\tau+T} e^{j\left\{\pi n\Delta f t^2+2\pi n(f_0-\Delta f\tau)t-2\pi n f_0\tau+\pi n\Delta f\tau^2+\phi_n(\tau)\right\}}e^{-j2\pi f t}dt\,+ \\
&\quad \frac{A_n(\tau)}{2}\int_{\tau}^{\tau+T} e^{-j\left\{\pi n\Delta f t^2+2\pi n(f_0-\Delta f\tau)t-2\pi n f_0\tau+\pi n\Delta f\tau^2+\phi_n(\tau)\right\}}e^{-j2\pi f t}dt
\end{aligned}
$$

We know that,

$$
\int e^{-(at^2+2bt+c)}dt = \frac{1}{2}\sqrt{\frac{\pi}{a}}e^{\frac{b^2-ac}{a}}erf\left(\sqrt{a}t+\frac{b}{\sqrt{a}}\right)+C \tag{2–14}
$$

where C is an arbitrary constant and erf is the error function, defined as,

$$
erf(t) = \frac{2}{\sqrt{\pi}}\int_0^t e^{-u^2}du \tag{2–15}
$$

From 2–14,

$$
Y_n(f,\tau) = \frac{A_n(\tau)}{2}\int_{\tau}^{\tau+T} e^{-(a_1t^2+2b_1t+c_1)}+e^{-(a_2t^2+2b_2t+c_2)}dt \tag{2–16}
$$

where

$$
\begin{aligned}
a_1 &= -j\pi n\Delta f & a_2 &= -jn\pi\Delta f \\
b_1 &= -j\pi(nf_0-n\Delta f\tau-f) & b_2 &= j\pi(nf_0-n\Delta f\tau+f) \\
c_1 &= -j\left\{(\pi n\Delta f\tau^2-2\pi n f_0\tau+\phi_n(\tau)\right\} & c_2 &= j\left\{(\pi n\Delta f\tau^2-2\pi n f_0\tau+\phi_n(\tau)\right\}
\end{aligned}
$$

Hence,

$$
\begin{aligned}
&Y_n(f,\tau) = \\
&\quad \frac{A_n(\tau)}{2}\frac{1}{2}\sqrt{\frac{1}{-jn\Delta f}}e^{j\left\{-2\pi f\tau-\pi(f-nf_0)^2/n\Delta f+\phi_n(\tau)\right\}} \\
&\quad \cdot\left\{erf\left(\frac{j\pi(f-nf_0-nT\Delta f)}{\sqrt{-j\pi n\Delta f}}\right)-erf\left(\frac{j\pi(f-nf_0)}{\sqrt{-j\pi n\Delta f}}\right)\right\}+ \\
&\quad \frac{A_n(\tau)}{2}\frac{1}{2}\sqrt{\frac{1}{-jn\Delta f}}e^{-j\left\{-2\pi f\tau-\pi(f+nf_0)^2/n\Delta f+\phi_n(\tau)\right\}} \\
&\quad \cdot\left\{erf\left(\frac{j\pi(f+nf_0+nT\Delta f)}{\sqrt{-j\pi n\Delta f}}\right)-erf\left(\frac{j\pi(f+nf_0)}{\sqrt{-j\pi n\Delta f}}\right)\right\}
\end{aligned}
$$

Similarly to $Y_n(f,\tau)$, we take a Fourier transform of $x_n(t)$ from Equation 2–8. $X_n(f)$ becomes

$$
\begin{aligned}
&X_n(f) = \\
&\quad \frac{1}{2}\left[\frac{1}{2}\sqrt{\frac{1}{-jn\Delta f}}e^{j\left\{-\pi(f-nf_0)^2/n\Delta f\right\}}\left\{erf\left(\frac{j\pi(f-nf_0-nT\Delta f)}{\sqrt{-j\pi n\Delta f}}\right)-erf\left(\frac{j\pi(f-nf_0)}{\sqrt{-j\pi n\Delta f}}\right)\right\}\right]+ \\
&\quad \frac{1}{2}\left[\frac{1}{2}\sqrt{\frac{1}{-jn\Delta f}}e^{-j\left\{-\pi(f+nf_0)^2/n\Delta f\right\}}\left\{erf\left(\frac{j\pi(f+nf_0+nT\Delta f)}{\sqrt{-j\pi n\Delta f}}\right)-erf\left(\frac{j\pi n(f+nf_0)}{\sqrt{-j\pi n\Delta f}}\right)\right\}\right]
\end{aligned}
$$

Therefore,

$$
H_n(f,\tau)=\frac{Y_n(f,\tau)}{X_n(f)}=A_n(\tau)e^{j\{-2\pi f\tau+\phi_n(\tau)\}}\sqcap\left(\frac{f-nf_0}{nT\Delta f}-\frac{1}{2}\right) \tag{2–17}
$$

Then the impulse response, $h_n(t,\tau)$, is

$$
\begin{aligned}
h_n(t,\tau) &= \mathcal{F}^{-1}\left[H_n(f,\tau)\right] && \text{(2–18)}\\
&= \int_{-\infty}^{\infty} H_n(f,\tau)e^{j2\pi ft}df && \text{(2–19)}\\
&= \int_{nf_0}^{nf_0+nT\Delta f} A_n(\tau)e^{j(-2\pi f\tau+\phi_n(\tau))}e^{j2\pi ft}df && \text{(2–20)}\\
&= A_n(\tau)e^{j\phi_n(\tau)}\int_{nf_0}^{nf_0+nT\Delta f} e^{j2\pi f(t-\tau)}df && \text{(2–21)}\\
&= A_n(\tau)e^{j\phi_n(\tau)}e^{j2\pi f_c(t-\tau)}sinc\left\{nT\Delta f(t-\tau)\right\}nT\Delta f && \text{(2–22)}
\end{aligned}
$$

where f_c is a center frequency of the frequency ramp.

So we find $h_n(t)$ by,

$$h_n(t) = \int_{-\infty}^{\infty} A_n(\tau) e^{j\phi_n(\tau)} e^{j2\pi f_c(t-\tau)} sinc\left\{nT\Delta f(t-\tau)\right\} nT\Delta f d\tau \qquad (2–23)$$

Recognizing the convolution integral, we may express $h_n(t)$ as:

$$h_n(t) = A_n(t) e^{j\phi_n(t)} * \left\{e^{j2\pi f_c t} sinc\left\{nT\Delta ft\right\} nT\Delta f\right\} \qquad (2–24)$$

which is equivalent to Equation 2–10.

2.4 TOA Properties

2.4.1 Timing Accuracy

One main concern regarding the TOA method is the timing accuracy of the detected peak amplitude. The effective impulse response is a sampled version of the continuous impulse response convolved with a sinc function whose width is determined by the bandwidth of the transmission. While the detected peak amplitude may be interpolated in time using standard Fourier techniques, the detected peak amplitude may not exactly coincide with the timing of the actual peak amplitude incident upon the receiver, due to convolution with the sinc function. To assess this accuracy, we calculate the Cramér-Rao Lower Bound (CRLB) [*Schuster et al.*, 2006, and reference therein] using the output of a modulated HF heating model that predicts the time distribution of amplitude and phase generated by modulated HF heating of the lower ionosphere. We now describe the HF heating model and how it is used to calculate the CRLB.

The HF heating model employed was developed by *Moore* [2007], and it requires as input the HF frequency, modulation frequency, and HF power. Electron temperature and density profiles, together with molecular nitrogen and molecular oxygen density profiles, are also provided as input. We apply the electron density profiles used in previous ELF/VLF studies [e.g., *Lev-Tov et al.*, 1995; *Moore*, 2007] and the rest of the ionospheric parameters are available in MSISE-90 Model provided by the Goddard Space Flight

Centers Space Physics Data Facility on the website at http://modelweb.gsfc.nasa.gov/. Using this input, the model computes the modulated conductivities (Perdersen, Hall and Parallel) at each 1 km grid in 3-D rectangular coordinates. Lastly, the model assumes a constant Electrojet electric field parallel to ground throughout the D-region ionosphere to predict the magnetic field incident upon a given receiver location as a function of time assuming free-space propagation [*Payne et al.*, 2007]. For example, the model may be used to predict the amplitude and phase of the magnetic field incident upon a receiver as a function of time using a modulation frequency of 2.5 kHz, an HF power of 85.7 dBW, and an HF frequency of 3.2 MHz (with X-mode polarization). The propagation model employed neglects Earth-ionosphere waveguide effects, however. For the receiver locations used in this work (each less than $\sim$100 km away from the HAARP transmitter), this assumption is reasonable as has been demonstrated by *Payne et al.* [2007], which showed excellent agreement between simple ray-tracing and full-wave modeling results at these distances. Applying the TOA technique to the predicted magnetic field time series, we are able to assess the timing accuracy of our peak TOA measurement. Each time bin has three unknown parameters: amplitude, phase, and time delay. We create the Fisher information matrix [*Schuster et al.*, 2006, and reference therein] which may be used to directly compute the CRLB for different white Gaussian Noise levels. Figure 2-2 shows the CRLB of the standard deviation of the time delay for the peak amplitude in the model as a function of the signal-to-noise ratio (SNR). Typically, the SNR of our observations is 5 dB or higher, and Figure 2-2 indicates a best-case accuracy of $\sim$1 μsec at 5 dB SNR. While model predictions using other ionospheric profiles may yield slightly different results than presented here, we expect the $\sim$1-μsec accuracy figure to be generally representative of the accuracy of the TOA measurement. Although ELF/VLF data is also sensitive to impulsive noise (from lightning, for example) and to power line radiation in the ELF/VLF range, the CRLB is still a reasonable benchmark for timing accuracy, since the integration period is large (typically $>$100 seconds). In addition to the error factors discussed above, there is a 27.5$\pm$2.5 μsec transmission delay due to the HAARP transmission and $\pm$30 $n$sec GPS accuracy, which have been accounted for in our analysis.

To experimentally evaluate the SNR of the measurement, we perform the same TOA analysis on the data set starting with an offset of 2 seconds. Because the frequency-time ramp is 4 seconds in duration, we do not expect HAARP-generated ELF/VLF waves to contaminate this measurement, yielding an effective measurement of the noise floor. From among the many noise-floor measurements that the TOA analysis produces, we pick the highest noise measurement as the noise floor. As an example, Figure 3-1 exhibits an approximate SNR of $\sim$12 dB (marked with a horizontal line) for the peak amplitude at Sinona Creek and an approximate SNR of $\sim$25 dB (marked with a horizontal line) for the peak amplitude at Milepost 71, both evaluated using 2.5 minutes of data. The nulls in the noise line may be caused by the hum noise interference. We note that the SNR of the measurement increases significantly by repeating the frequency-time ramps for a few minutes.

2.4.2 Timing Resolution

Although the timing accuracy is not significantly limiting, the time resolution of the TOA method is more significant. Timing resolution may be analyzed using standard Fourier techniques, and it is limited by the bandwidth of the received signal. For example, a signal bandwidth of 4kHz provides a time resolution of 250 μsec, since only positive frequencies are used in the analysis. As a result, this TOA method cannot fully resolve signals arriving within 250 μsec of each other. Nonlinear deconvolution techniques are available and have been employed to surpass this limit, however, as will be discussed in Section 3.1.

2.4.3 Previous TOA Analysis

The TOA method presented herein is similar in many regards to previous work analyzing the effective source height of ELF/VLF waves generated by modulated HF heating. *Rietveld et al.* [1989] demonstrated a method to determine the group delay of the ELF/VLF signal received on the ground as a function of modulation frequency. Measurements of ELF/VLF signals generated using a linear frequency-time modulation format were used to calculate the change in received phase per change in frequency, which is directly related to the overall group delay. Assuming the ELF/VLF source is located directly above the HF transmitter, *Rietveld et al.* [1989] calculated the 'apparent source height' of the ELF/VLF source region as a function of modulation frequency, although the application of this method to experimental data produced source region altitudes varying rapidly as a function of frequency between 60 and 130 km as is shown in Figure 2-3. *Riddolls* [2003] applied a similar TOA method to ELF/VLF harmonics generated during the HF heating process, but the underlying method remained the same as that described by *Rietveld et al.* [1989].

The new TOA method described in this work utilizes linear frequency-time modulation ramps, similar to *Rietveld et al.* [1989], but does not directly rely upon a calculation of the measured phase differential with frequency. Instead, the presented method focuses on the calculation of an effective impulse response of the system. The time resolution attained is sufficient to distinguish between line-of-sight ELF/VLF signals and ionospherically-reflected ELF/VLF signals and our results indicate that ionospherically-reflected propagation paths likely affect the calculations presented by both *Rietveld et al.* [1989] and *Riddolls* [2003].

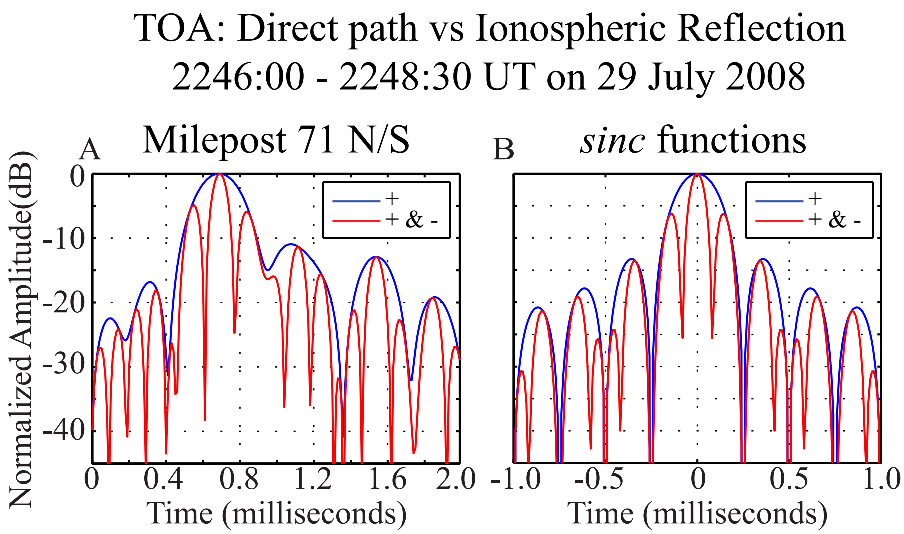

Figure 2-1. A) TOA observations : The amplitudes of the received ELF/VLF signal as a function of time at Milepost 71 NS antenna. B) Convolved sinc functions : The amplitudes of sinc functions being convolved shown in Equation 2–9. Each blue line is a result of using only positive frequency component in Equation 2–9 and each red line is a result of using both positive and negative frequency components.

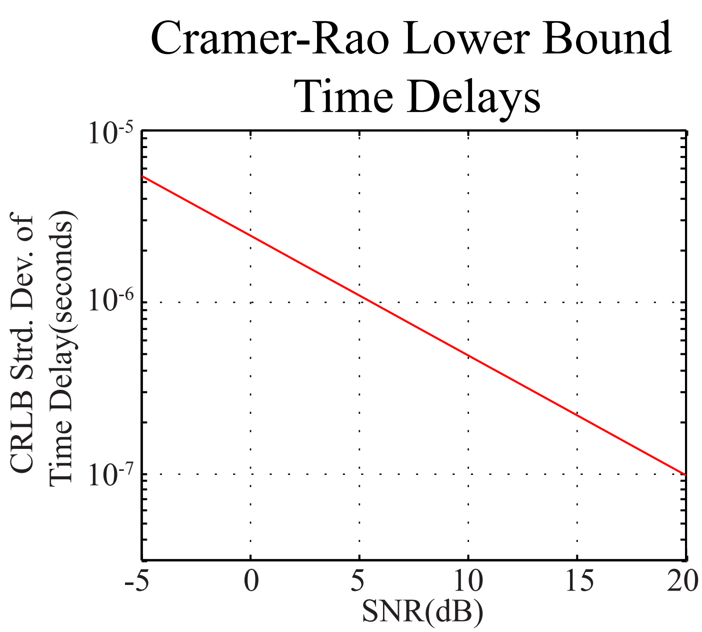

Figure 2-2. Cramér-Rao Lower Bound (CRLB) of the standard deviation of the time delay for the peak amplitude computed by the HF heating model.

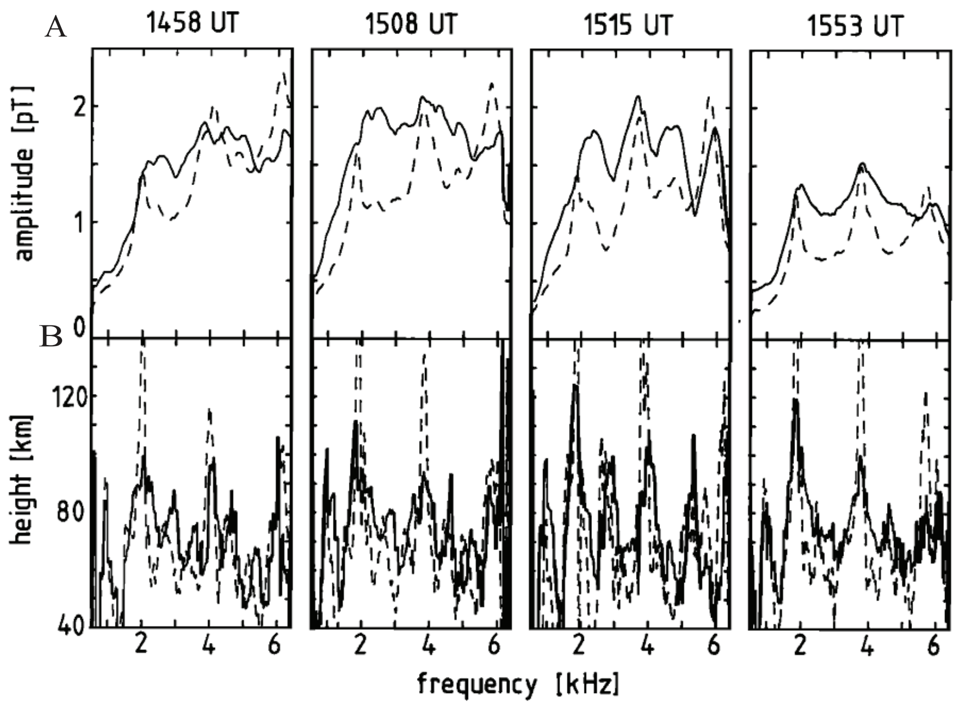

Figure 2-3. Experimental Observations. A) the amplitudes of the received ELF/VLF waves. B) ‘apparent source height’ at Tromsø on November 8, 1984 presented by M.T.Rietveld et al. ŤOn the frequency dependence of ELF/VLF waves produced by modulated ionospheric heatingŤ,Radio Sci.,vol.24,no.3, pp.270-278,1989

CHAPTER 3
TOA OBSERVATION AND ANALYSIS

In this chapter, we provide the TOA analysis of ELF/VLF signal observations for various HF heating schemes. We demonstrate that the ELF/VLF TOA technique is a valid experimental measurement of the amplitude and phase of the received ELF/VLF signals as a function of time. Section 3.1 compares experimental TOA observations with model predictions and Section 3.2 experimentally demonstrates the TOA sensitivity to different HF heating parameters.

3.1 Comparison with Model

Example TOA results are provided in Figure 3-1 for data acquired on 29 July 2008. During this experiment, a 7x7 element sub-array of the HAARP facility radiated at 3.2 MHz (X-mode) modulated with frequency-time ramps from 1 to 5 kHz over a period of 4 seconds. These frequency-time ramps were repeated sequentially for 150 seconds. Figure 3-1 shows the TOA observations at Sinona Creek (SC) and Milepost 71 (MP71) in the North-South (NS) antenna together with the approximated noise floor, demonstrating that the transmission sequence may be used to produce observations with significant SNR ($\sim$12 dB at SC and $\sim$25 dB at MP71). Figure 3-2 compares these same observations with model predictions. The solid blue lines are experimental observations; the solid red traces are the predicted amplitudes as a function of time (without processing, but including ionospheric reflection) with the reflection height set at 65 km and the effective reflection coefficient set at $0.3\angle 150^{\circ}$; and the dashed red lines represent the predicted amplitudes as a function of time (following TOA processing). The solid green spikes in Figure 3-2 are derived from observations and calculated using a nonlinear deconvolution method known as the CLEAN method [*Segalovitz and Frieden*, 1978], and the dashed green traces are the results of TOA processing on these CLEAN method extractions. The CLEAN method iteratively subtracts a portion of the largest amplitude signal from the TOA observations until the noise floor is reached. The CLEAN method thus decomposes the observed TOA into a series of complex-valued δ functions. We interpret earlier arrival times (e.g., $\sim$573 μ seconds at SC and $\sim$673 μ seconds at MP71) as the result of line-of-sight, or direct-path, propagation, whereas we interpret later arrival times (e.g., $\sim$900 μ seconds at SC and $\sim$1.04 milliseconds at MP71) as the result of ionospherically-reflected-path propagation.

After de-convolving using the CLEAN method, several outliers may exist that defy physical interpretation. For instance, at intermediate stages, the process of subtracting the largest amplitude sinc function may create false peaks at times earlier than the speed-of-light propagation time from the transmitter to the receiver. We remove these times from the CLEAN output and determine the amplitude and phase at permissible arrival times using a regularized least-squares fit to the complex-valued impulse response. For example, at Milepost 71 in Figure 3-2, the CLEAN method extracts several pulses from the observed TOA. Pulses arriving earlier than 320 μsec (corresponding to the 96 km line-of-sight propagation path from HAARP to the receiver) are removed from the series. The amplitude and phase of the remaining pulses pulses are then determined using a regularized least-squares fit to the impulse response (solid blue trace).

Figure 3-2 shows that the modeled direct-path TOA reasonably matches the observed TOA at both SC and MP71. The TOA of the ionospherically-reflected components at MP71 also closely match the timing of the model results, although at SC, the model and observed data are not aligned in time. This is possibly due to the low SNR of the ionospherically-reflected component in SC data (see Figure 3-1). It may also be possible that the ionospherically-reflected components observed at SC and MP71 have reflection heights and/or reflection coefficients due to the different angles of incidence at the ionospheric boundary. This example, and particularly the MP71 observation, demonstrates the ability of the TOA technique to discern between direct-path and ionospherically-reflected path components of the ELF/VLF waves observed at the receiver. It also demonstrates the ability to assign amplitude (and phase, not shown) values as a function of time. Both experimental observations and the HF heating model indicate that the time difference between the direct and ionospherically-reflected signal paths is greater than $\sim$400 μsec, implying a bandwidth of $\sim$2.5 kHz is suitable to resolve the two peaks.

3.2 Beam Direction

During the Summer Student Research Campaign (SSRC) at HAARP on August 6th and 7th, 2009, the University of Florida conducted ELF/VLF wave generation experiments to evaluate the ELF/VLF TOA as a function of HF beam direction. Unlike the TOA experiments discussed above, the modulation format consisted of frequency-time ramps ranging between 1.5 and 3.5 kHz over a period of 4 seconds (i.e., a smaller bandwidth). The HF transmitter aimed in three directions: 5° off-zenith toward Sinona Creek, vertical, and 5° off-zenith away from Sinona Creek (azimuth 56.8°). A 5° shift in the location of the ELF/VLF source region corresponds to a $\sim$9 km lateral offset at 100 km altitude, and only a 2–4 km difference in total ranging (from HAARP to the ionosphere to the receiver). This experiment was designed to investigate whether the TOA method is sensitive to this relatively small spatial shift in the ELF/VLF source location.

The top panel of Figure 3-3 shows the TOA results for individual antennas at Sinona Creek and Milepost 71. At Milepost 71, the arrival times for each of the HF beam directions are in the order expected. At Sinona Creek, however, on the NS antenna, ELF/VLF waves generated using the vertical HF beam arrive first, followed by those generated using the “Away” beam, followed by those generated using the “Toward” beam: a counter-intuitive result. This discrepancy results from the interference between TOA results for the Hall and Pedersen currents, and thus on the direction of the auroral electrojet. For instance, the bottom panel of Figure 3-3 shows the *magnitude* of the TOA analysis and yields the intuitive result at both Sinona Creek and Milepost 71: the dominant TOA is in the order of the shortest propagation time to the longest. In addition to the ordering being correct, the TOA differences between the traces are clearly evident, indicating that the TOA method is able to detect the peak arrival time with high ranging accuracy (<2–3 km).

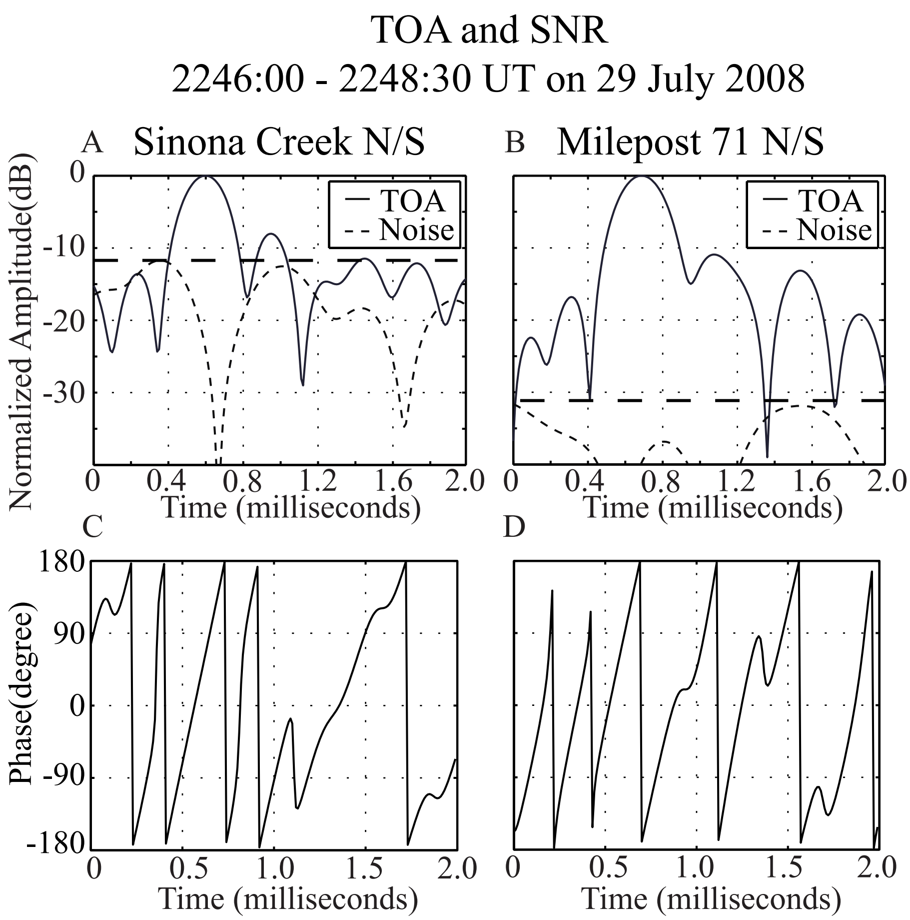

Figure 3-1. TOA observations: The amplitudes and phase of the received ELF/VLF signal as a function of time. A) and C) Sinona Creek NS antenna. B) and D) Milepost 71 NS antenna. The dashed line in each case shows the approximate noise level for each site. The horizontal wide dashed line is our noise reference level determined the peak approximated noise level. The reference noise level is used to estimate SNR of the detected ELF/VLF signals.

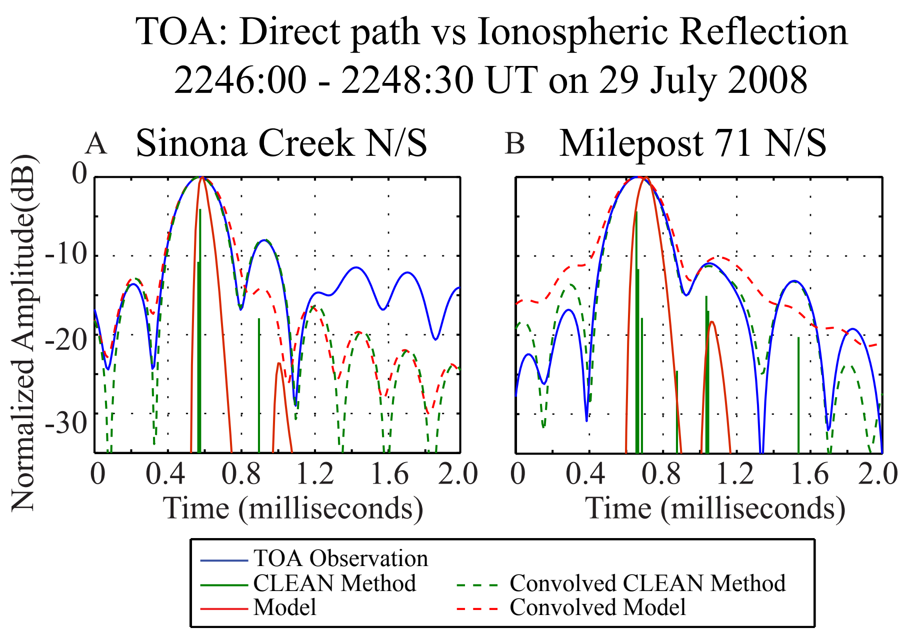

Figure 3-2. A Comparison between model prediction and observations: A) Sinona Creek. B) Milepost 71. On this plot, we use the CLEAN method with the gain loop 0.4.

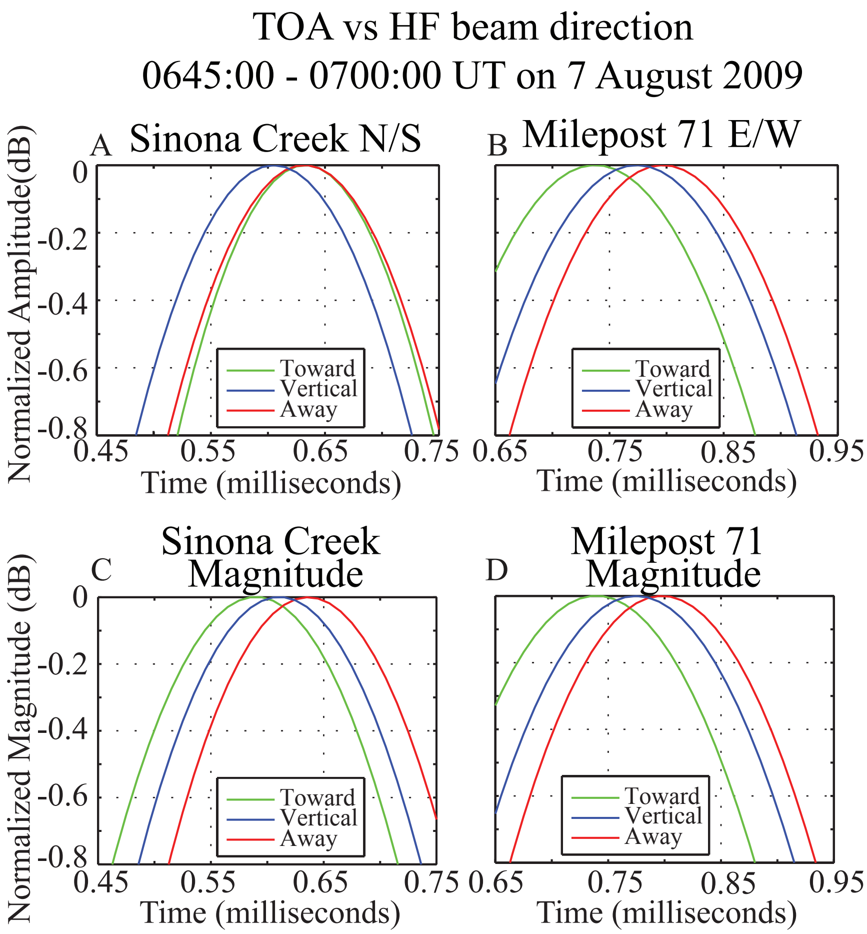

Figure 3-3. TOA vs HF beam direction: TOA using a single antenna. A) Sinona Creek. B) Milepost 71. TOA of the ELF/VLF signal magnitude. C) Sinona Creek. D) Milepost 71.

CHAPTER 4
GEOPHYSICAL INTERPRETATION

Thus far, we have described the details of TOA signal processing, and we have provided proof-of-concept experimental results using simple experiments. In this chapter, we use TOA processing to provide geophysical interpretations of more complicated experiments.

4.1 Dual-Beam Experiment

The Dual-Beam HF heating experiment utilizes a novel HF transmission scheme at HAARP together with TOA analysis to estimate the location of the dominant ELF/VLF source region in 2-D. In addition to the TOA, this experiment estimates the off-zenith angle of the dominant source location. The Dual-Beam heating experiment transmits two different HF signals toward the ionosphere at the same time. As is depicted in Figure 4-1, one side of the HAARP transmitter array heats the ionosphere using Amplitude Modulation (AM) while the other side heats using a Continuous Wave (CW) beam with varying off-zenith angles. *Moore and Agrawal* [2011] proved that CW heating in addition to modulated heating reduced the ELF/VLF amplitude received on the ground. The CW beam effectively probes the larger modulated region to determine the off-zenith heating angle that reduces the received ELF/VLF amplitude the most, identifying the dominant ELF/VLF source region.

4.1.1 Experiment Description

The Dual-Beam experiment was performed on July 29th, 2008 followed by the TOA experiment introduced in Section 3.1 in the previous chapter. The Dual-Beam experiment split the 12x15 transmitter array in to two sub-arrays. One 7x7 sub-array modulates the electrojet currents at 2485 Hz using square-wave Amplitude Modulation (AM) at 3.2 MHz (X-mode) while the other 8x8 sub-array simultaneously heats smaller portions of the modulated region using a 9.5 MHz Continuous Wave (CW) beam (X-mode). The zenith angle of the 9.5 MHz CW beam is stepped between 0° and 15°. For

30 seconds, as the CW beam turns on and off every two seconds, the off-zenith angles change discretely for two second intervals in the following values: 0°, 2°, 4°, 6°, 9°, 11°, 13° and 15°. The azimuths (East of North) of the CW beam were directed toward each receiver site, 48.84° for Sinona Creek, and 56.76° for Milepost 71.

4.1.2 Experimental Results

Figure 4-2 shows the variations in the normalized ELF/VLF amplitude as function of the CW heating beam angle. The off-zenith angle that minimizes the normalized amplitudes are different at Sinona Creek and Milepost 71. We approximate the amplitude-minimizing zenith angle as 2.5° - 5.0° for Sinona Creek and as 9.5° - 12.0° for Milepost 71 as is shown as gray swaths in Figure 4-2.

Using the simple geometry show in Figure 4-1, the amplitude-minimizing zenith angle from the Dual-Beam Heating experiment, and the total propagation delay time from the TOA experiment, we may determine the ELF/VLF generation source region. The height h and radial distance r of the ELF/VLF source location is expressed by

$$h = \frac{(R^2 - D^2)\cos\alpha}{2(R - D\sin\alpha)} \tag{4–1}$$

$$r = h\tan\alpha = \frac{(R^2 - D^2)\sin\alpha}{2(R - D\sin\alpha)} \tag{4–2}$$

where R is the total propagation distance and α is the zenith angle. D is the distance between the transmitter and receiver. R is determined assuming speed-of-light propagation and using the arrival time of peak TOA magnitude in Figure 3-1 (with the known errors discussed in Section 2.4.1). The error from the zenith angle and total propagation distance results in different ranging accuracies at Sinona Creek and Milepost 71 shown in Table 4-1. The error in Table 4-1 is an average side length of the approximate ELF/VLF source region. Additionally, the intersection of the approximated zenith angle and the ellipse drawn by the ELF/VLF total propagation distance determines 2-D ELF/VLF wave source region as is shown in Figure 4-3. The filled areas in Figure 4-3 correspond to the dominant ELF/VLF source region in each case.

From these experimental results, we make two observations: The dominant ELF/VLF source regions are located at approximately same altitude, and they increase with radial distance from the center of the modulated HF beam the farther away the receiver is from the transmitter. The dominant source altitude is in a range of previous observations *James* [1985] and *Rietveld et al.* [1986]. From these experimental results, we expect the lateral dominant source location is a function of receiver site.

4.2 TOA vs VLF Frequency

In the previous sections, we applied TOA analysis to estimate the dominant ELF/VLF source location. In this section, we limit the frequency range and analyze the received signal dependence on modulation frequency.

4.2.1 Experiment Description

On 22 July 2010, during the 2010 Polar Aeronomy and Radio Science (PARS) Summer School, the full 12x15 HF array broadcast at 3.25 MHz (X-mode) frequency-time modulation ramps ranging from 1 to 5 kHz over a period of 8 seconds (repeated 10 times). Observations were performed at Sinona Creek and at Paradise using TOA analysis. For this analysis, we limited the bandwidth to 3 kHz and calculated the TOA (attributed to the center frequency of the bandwidth) for center frequencies between 2.5 and 3.5 kHz.

4.2.2 Experiment Results and Anlaysis

Figure 4-4 shows the TOA variations as a function of center frequency for Sinona Creek and Paradise together with the modeled Hall conductivities as a function of height in the bottom panel. The plotted times in the figure are computed by the CLEAN method and regularized fitting as are described in Section 3.1 to ensure a valid separation of the direct and ionospherically-reflected path signals. Then we find the arrival times of the dominant direct path signal with the ideal interpolation.

The TOA clearly decreases with increasing center frequency at both Sinona Creek and Paradise. This relationship is not unexpected. To illustrate this effect, the bottom panel of Figure 4-4 shows the altitude profile of conductivity modulation directly above the HAARP transmitter for 1 kHz and 5 kHz modulation. The variation in the two traces is almost exactly the same below 85 km altitude. Above 85 km, 1 kHz modulation is relatively stronger than 5 kHz modulation. The modulation of the Pedersen conductivity (not shown) exhibits similar effects. An overall reduction in altitude with increasing modulation frequency results, and this reduction in altitude brings about a shorter propagation delay to the receiver.

4.3 TOA vs High Frequency (HF) and Power

4.3.1 Experiment Description

During the Basic Research on Ionospheric Characteristics and Effects (BRIOCHE) Campaign at HAARP in June 2010, the University of Florida conducted ELF/VLF generation experiments to investigate the TOA as a function of HF frequency and HF power. The frequency-time ramps in this case ranged from 1 to 5 kHz over a period of 4 seconds. Every 4 second period, the HF power alternated between 25%, 50% and 100% power, and each period repeated for 5 minutes. Every 5 minutes, the HF frequency switched betweeen 3.2 MHz (X-mode) and 5.8 MHz (X-mode). Observations were performed at Sinona Creek and at Milepost 71, but the introduction of commercial powerlines near Milepost 71 site has significantly reduced the data quality at that site. In this section, only observations from Sinona Creek will be discussed.

4.3.2 Experiment Results and Anlaysis

Figure 4-5 shows the TOA for the maximum peak magnitude as a function of HF power at 3.2 MHz and at 5.8 MHz. The variations in TOA are small, less than 10 μseconds, whether in terms of HF frequency or in terms of HF power. The experimental results presented in Figure 4-5 do not definitively exhibit a monotonic increase in the TOA in terms of the HF power, and neither do they definitively show an increase in the TOA from 3.2 MHz to 5.8 MHz. Nevertheless, it is clear that the effects of HF frequency and power are relatively small compared to other parameters, such as the HF beam direction. It will be necessary to complete a full statistical analysis of HF power and HF frequency TOA observations to determine whether a consistent dependence may be derived from this data set.

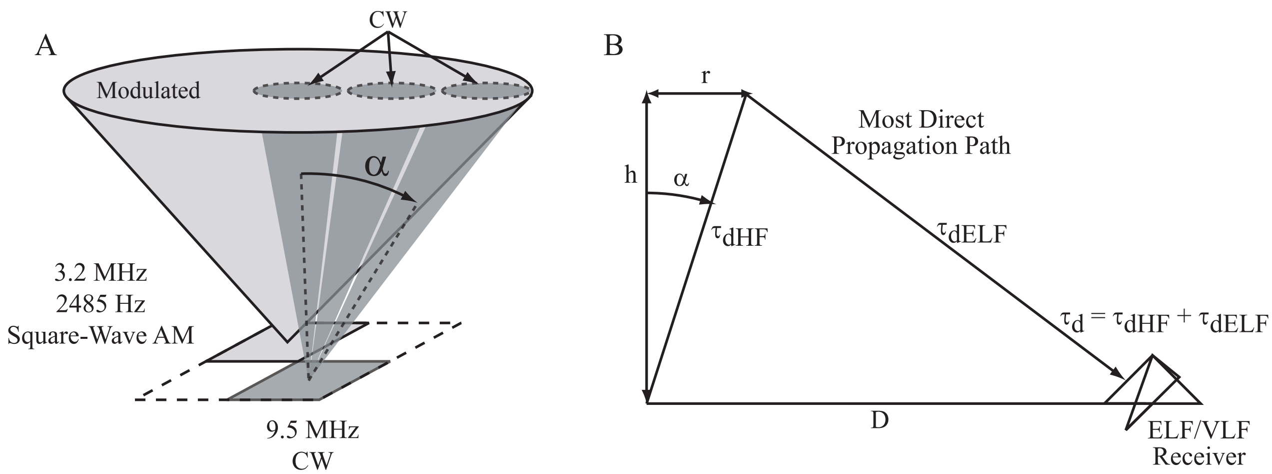

Figure 4-1. Cartoon diagram of the Dual-beam experiment. A) Half of the transmitters heats the ionosphere using the amplitude modulation while the other half simultaneously heats with the CW beam. B) Simple geometry for direct propagation path

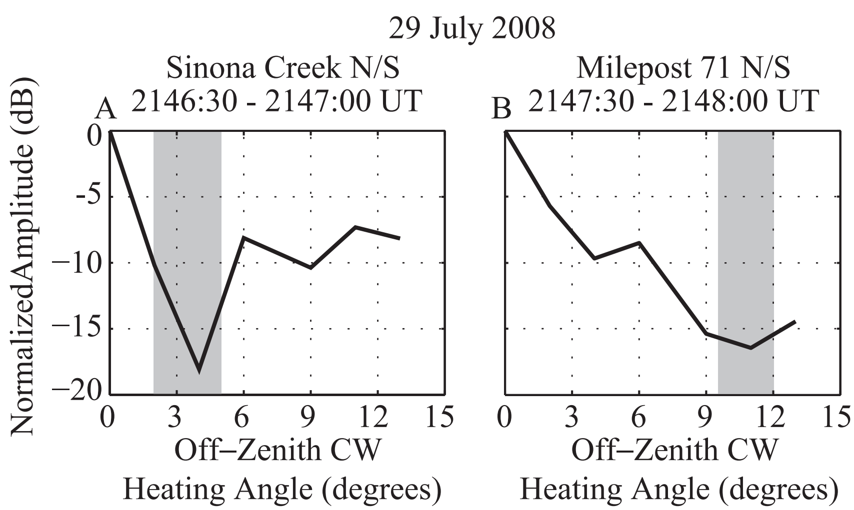

Figure 4-2. Dual-beam heating observations: Normalized amplitudes of the observed ELF/VLF signals as a function of the off-zenith CW heating angle. A) Sinona Creek. B). Milepost 71. The azimuth of the CW beam was aligned with Sinona Creek between 2146:30 and 2147:00 UT and was aligned with Milepost 71 between 2147:30 and 2148:00 UT on 29 July 2008

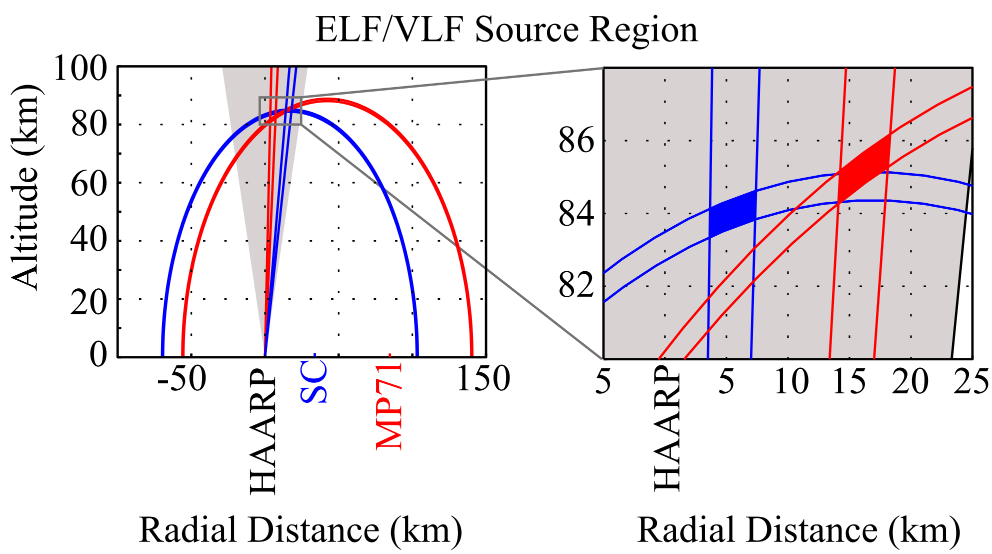

Figure 4-3. Dominant ELF/VLF source region map: TOA maximum magnitude ellipse drawn together with dual-beam minimization zenith angles for Sinona Creek (red) and for Milepost 71 (blue) respectively. The filled colored areas represent the dominant ELF/VLF region in each case while the gray area represents the HF heated region.

Table 4-1. ELF/VLF source region

Receiver	Altitude (km)	Radius (km)	Error (km)
Sinona Creek	83.3 - 84.6	3.65 - 7.40	2.21
Milepost 71	84.3 - 86.2	14.1 - 18.3	2.82

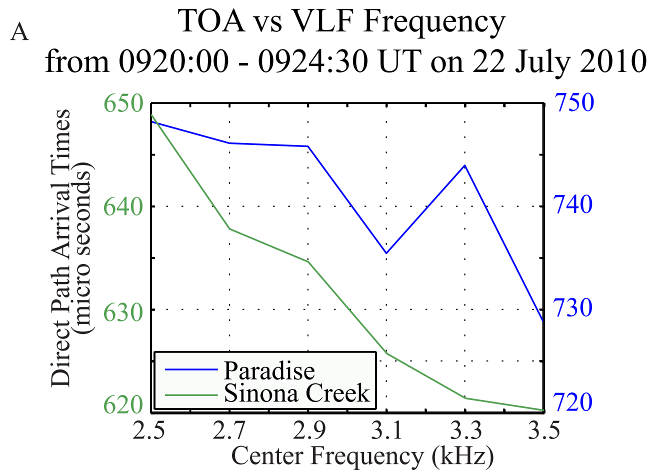

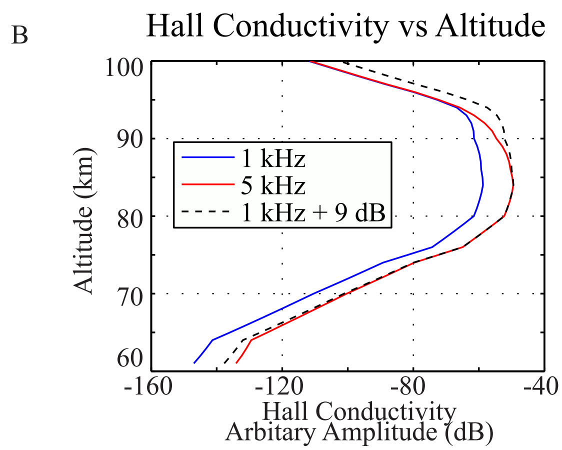

Figure 4-4. A) TOA as a function of ELF/VLF frequency : The Green line is the TOA for Sinona Creek and the Blue line for Paradise. B) Hall conductivity modulation amplitude as a function of height with different VLF frequencies : The blue line is with the VLF frequency of 1 kHz and the red line is of 5 kHz. This model is generated by using a medium electron density profile, 3.2 MHz HF frequency and full HF power with 12x15 array at HAARP.

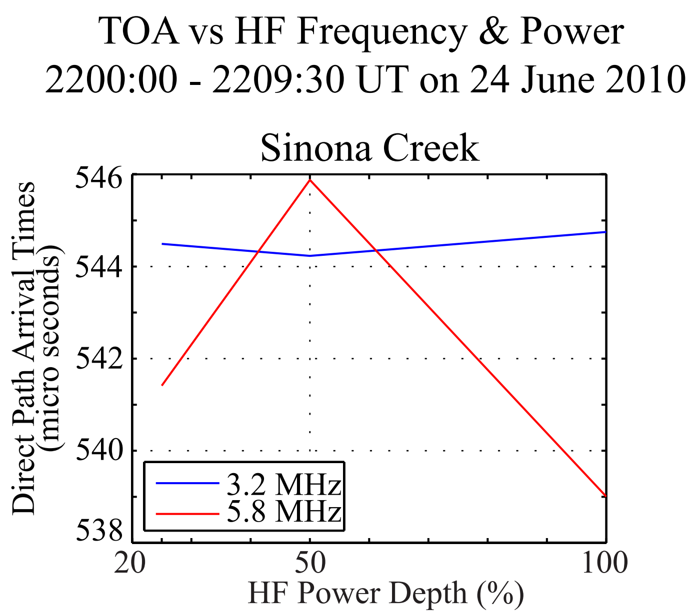

Figure 4-5. TOA as a function of HF frequency and power at Sinona Creek. The TOA of the maximum magnitude is plotted as a function of HF power with different HF frequencies.

CHAPTER 5
SUMMARY AND FUTURE WORK

5.1 Summary

This thesis examines ELF/VLF wave generation by modulated HF hating of the lower ionosphere. A new TOA analysis technique has been applied to ELF/VLF wave observations.

Utilizing frequency-time ramp modulations, we measure the amplitude and phase of the ELF/VLF waves as a function of time at the receiver. This signal scheme has been applied in radar applications and are known to be highly accurate measurements [*Schuster et al.*, 2006]. The ELF/VLF TOA analysis succeeds in 1) distinguishing a direct and ionospherically-reflected path signals and 2) estimating the dominant ELF/VLF source region, which is shown to be dependent on the receiver location and the ELF/VLF (modulation) frequency, but not significantly on the HF power and frequency.

5.2 Future Work

5.2.1 TOA Analysis for HF beams at Different Azimuths

As is discussed in Section 3.2, the TOA observations are sensitive to the HF beam direction. In future experiments, we may also tilt the HF beam at different azimuths and apply the TOA analysis. As *Payne et al.* [2007] predicts from his HF heating and ELF/VLF propagation model, the current source directions may be found as the beam rotates in azimuth using ELF/VLF vertical Electric field data. He also mentioned that a HAARP-collocated receiver would estimate the current source directions using the ground based magnetic field data. His suggestion is derived from the free space propagation in Equation 1–7, therefore, isolation of direct path signals from ionospherically-reflected path signals using TOA analysis may be helpful to his estimation method.

5.2.2 TOA Analysis for Different HF Beam Patterns

HAARP is capable of transmitting various HF beam patterns, such as broad-, narrow-, and donut-shaped patterns [*Cohen*, 2009; *Leyser et al.*, 2009]. As is introduced in *Cohen* [2009], the broad shaped HF beams can extend into different directions. Different HF beam patterns result in different ELF/VLF wave generation efficiencies, and it is at present not well understood why this is the case. TOA analysis may be applied to determine how the dominant ELF/VLF source region depends on the HF beam pattern. Considering saturation effect in the ELF/VLF generation [*Moore*, 2007], the broad HF beams may be more efficient than the narrow HF beams. However, the broad HF beams cause more interference of the generated ELF/VLF signals due to the phase spreading in the lager heated region [*Barr et al.*, 1998]. The donut-shape HF beam, on the other hand, has the peak HF energy away from the beam center. TOA analysis with the ability to range the source location and to separate multi-paths will be a convenient diagnostic tool to evaluate the ELF/VLF generation efficiency on these different HF beam shapes.

5.2.3 TOA Analysis for Different Modulation Techniques

In this thesis, we apply TOA analysis to amplitude modulated waveforms. As an alternative modulation method, the HF beam may move rapidly at the modulation frequency using the Continuous Waveform (CW) [*Cohen et al.*, 2008; *Papadopoulos et al.*, 1990]. Compared to the conventional amplitude modulation, this alternative modulation has a larger heated region and the interpretation of the signal interference becomes more complex. Although *Cohen et al.* [2008] claims the ”geometric modulation” increases the ELF/VLF wave generation efficiency, the TOA analysis may be useful to experimentally re-evaluate the efficiency including the interference effects and the dominant source regions.

REFERENCES

Balanis, C. A., *Advanced Engineering Electromagnetics*, John Wiley & Sons Inc, New York, 1986.

Barr, R., M. T. Rietveld, P. Stubbe, and H. Kopka, Ionospheric Heater Beam Scanning: A Realistic Model of This Mobile Source of ELF/VLF Radiation, *Radio Sci.*, *23*(3), 1073, 1998.

Barrick, D. E., Fm/cw radar signals and digital processing, *Tech. Rep. ERL283-WPL20*, NOAA, 1973.

Boashash, B., *Time frequency signal analysis and processing : a comprehensive reference*, 743 pp., Elsevier, Oxford, UK, 2003.

Budden, K. G., *The propagation of radio waves: the theory of radio waves of low power in the ionosphere and magnetosphere*, Cambridge University Press, Cambridge, UK, 1985.

Cohen, M. B., Elf/vlf phased array generation via frequency-matched steering of a continuous hf ionospheric heating beam, Ph.D. thesis, Stanford University, 2009.

Cohen, M. B., U. S. Inan, and M. G. kowski, Geometric modulation: A more effective method of steerable elf/vlf wave generation with continuous hf heating of the lower ionosphere, *Geophys. Res. Lett.*, *35*, L12101, doi:10.1029/2008GL0340610, 2008.

Cummer, S., U. Inan, and T. Bell, Ionospheric *D* region remote sensing using vlf radio atmospherics, *Radio Sci.*, *33*(6), 1781–1792, 1998.

Davies, K., *Ionospheric Radio*, Peter Peregrinus Ltd., London, UK, 1990.

Gabor, D., Theory of communication., *J. IEE*, *93*(26), 429–457, 1946.

Getmantsev, G. G., N. A. Zuikov, D. S. Kotik, L. F. Mironenko, N. A. Mityakov, V. O. Rapoport, V. Y. T. Y. A. Sazonov, and V. Y. Eidman, Combination frequencies in the interaction between igh-power short-wave radiation and ionospheric plasma, *JETP Lett*, *20*, 101–102, 1974.

James, H. G., The ELF spectrum of artificially modulated d/e-region conductivity, *J. Atmos. Terr. Phys.*, *47*(11), 1129–1142, 1985.

Lev-Tov, S. J., U. S. Inan, and T. F. Bell, Altitude profiles of localized *D* region density disturbances produced in lightning-induced electron precipitation events, *J. Geophys. Res.*, *100*(A11), 21,375–21,383, 1995.

Leyser, T., L. Norin, M. McCarrick, T. Pedersen, and B. Gustavsson, Radio pumping of ionospheric plasma with orbital angular momentum, *Phys. Rev. Lett.,*, *102*, 2009.

Moore, R. C., ELF/VLF wave generation by modulated HF heating of the auroral electrojet, Ph.D. thesis, Stanford University, Stanford, CA, 2007.

Moore, R. C., and D. Agrawal, ELF/VLF wave generation using simultaneous cw and modulted hf heating of the ionosphere, *J. Geophys. Res*, *116*, A04217, doi: 10.1029/2010JA015902, 2011.

Papadopoulos, K., C. Chang, P. Vitello, and A. Drobot, On the efficiency of ionospheric elf generation, *Radio Sci.*, *25*(6), 1990.

Papadopoulos, K., T. Wallace, M. McCarrick, G. M. Milikh, and X. Yang, On the efficiency of ELF/VLF generation using hf heating of the auroral electrojet,, *Plasma Phys. Rep.*, *29*, 2003.

Payne, J. A., U. S. Inan, F. R. Foust, T. W. Chevalier, and T. F. Bell, Hf modulated ionospheric currents, *Geophys. Res. Lett.*, *34*, L23101, doi:10.1029/2007GL031724, 2007.

Riddolls, R. J., Structure of the polar electrojet antenna, Ph.D. thesis, Massachusetts Institute of Technology, Cambridge, MA, 2003.

Rietveld, M. T., R. Barr, H. Kopka, E. Nielsen, P. Stubbe, and R. L. Dowden, Ionospheric heater beam scannning: A new technique for ELF studies of the autoral ionosphere, *Radio Sci.*, *19*(4), 1069–1077, 1984.

Rietveld, M. T., H. Kopka, and P. Stubbe, *D*-region characteristics deduced from pulsed ionospheric heating under auroral elecrojet conditions, *J. Atmos. Terr. Phys.*, *48*(4), 311–326, 1986.

Rietveld, M. T., P. Stubbe, and H. Kopka, On the frequency dependence of ELF/VLF waves produced by modulated ionospheric heating, *Radio Sci.*, *24*(3), 270–278, 1989.

Schuster, S., S. Scheiblhofer, L. Reindl, and A. Stelzer, Performance evaluation of algorithms for saw-based temperature measurement, *IEEE Trans. Ultrason., Ferroelectr., Freq. Control*, *53*, 1177–1185, 2006.

Segalovitz, A., and B. R. Frieden, A "CLEAN"-type deconvolution algorithm, *Astron. Astrophys. Suppl.*, *70*, 335–343, 1978.

Tomko, A. A., Nonlinear phenomena arising from radio wave heating of the lower ionosphere, Ph.D. thesis, The Pennsylvania State University, 1981.

Wait, J., The sanguine concept, in *Engineering in the Ocean Environment, Ocean 72 - IEEE International Conference on*, pp. 84 –87, doi:10.1109/OCEANS.1972.1161183, 1972.

BIOGRAPHICAL SKETCH

Shuji Fujimaru was born in Japan in 1986. He received a bachelor's degree in electrical and computer engineering from the University of Florida in 2009. With the Alumni Fellowship award from the University of Florida, he entered the Ph.D program in electrical and computer engineering. He received his master's degree on the way to the Ph.D. with guidance from Dr. Robert Moore. His research focuses on ELF/VLF generation using modulated HF heating of the lower ionosphere. His studies are mainly applied to electromagnetics, plasma physics, and signal processing.